



Thermal characteristics, kinetics, gas emissions and thermodynamic simulations of (co-)combustions of textile dyeing sludge and waste tea

Haiming Cai ^a, Jingyong Liu ^{a,*}, Jiahong Kuo ^{a,b}, Musa Buyukada ^c, Fatih Evrendilek ^{d,e}

^a Guangzhou Key Laboratory of Environmental Catalysis and Pollution Control, Guangdong Key Laboratory of Environmental Catalysis and Health Risk Control, School of Environmental Science and Engineering, Institute of Environmental Health and Pollution Control, Guangdong University of Technology, Guangzhou, 510006, China

^b Department of Safety, Health and Environmental Engineering, National United University, Miaoli, 36063, Taiwan

^c Department of Chemical Engineering, Bolu Abant Izzet Baysal University, Bolu, 14052, Turkey

^d Department of Environmental Engineering, Bolu Abant Izzet Baysal University, Bolu, 14052, Turkey

^e Department of Environmental Engineering, Ardahan University, Ardahan, 75002, Turkey

ARTICLE INFO

Article history:

Received 6 May 2019

Received in revised form

20 July 2019

Accepted 19 August 2019

Available online 19 August 2019

Handling Editor: Giorgio Besagni

Keywords:

Textile dyeing sludge

Waste tea

(Co-)combustion

Kinetics

Gas emissions

Ash components

ABSTRACT

The thermal conversion of waste into energy is increasingly becoming an integral part of environmentally friendly and sustainable societies. In this study, the (co-)combustion behaviors, kinetics, and gas emissions of textile dyeing sludge (TDS) and waste tea (WT) were quantified. The addition of WT appeared to avoid the drawbacks of both TDS and WT and to enhance their combustion efficiency. The main co-combustion process was characterized by three stages. The WT addition led to higher reactivity and a better combustion performance. The average apparent activation energy reached its minimum (154.82 kJ/mol) with 40% WT. The reaction mechanisms of the three stages of the 40% WT blend were best described using the D2, F3 and F2.3 models, respectively. The interaction between TDS and WT occurred between 370 and 550 °C. The WT addition changed the peak strength of Fe₂O₃ and produced NaAlSiO₄ and CaSO₄. The blend ash composition was found to consist of Fe₂O₃, CaSO₄, Na₂SO₄, Ca₅HP₃O₁₃, and NaAlSiO₄ according to X-ray diffraction analysis and thermodynamic simulations. The WT addition reduced SO₂ emission from the co-combustion. Our results can be benefited to provide pollution reduction, energy generation, performance improvement, scaling-up, and optimization for the industrial applications.

© 2019 Elsevier Ltd. All rights reserved.

1. Introduction

The textile industry is one of the most polluting ones due to the wastewater containing dyes pollution (Daneshvar et al., 2017; Tatarchuk et al., 2019) and the rapid generation rate of its textile dyeing sludge (TDS) (Peng et al., 2015). For example, the total generation amount of TDS was 21 million tons in China in 2015 (Xie et al., 2018). Both its increasing generation rate and complex chemical content such as organic dyes (Albadarin et al., 2017), and heavy metals render its traditional disposal methods such as landfilling, and ocean dumping obsolete nationally and globally (Wang et al., 2019b). Instead, high-tech (co-)combustion processes are being adopted owing to their advantages such as reductions in solid waste, land occupation, and environmental pollution, and

bioenergy generation (Guo and Zhong, 2018b), and the development of by-products (Sun et al., 2019). Due to its low calorific value and high ash content, TDS has low mono-combustion efficiency, and thus, is co-combusted with some auxiliary fuels such as biofeedstocks, or coals (Chen et al., 2015a; Huang et al., 2019).

Globally, biofeedstocks such as biomass residues, and energy crops meet about 14% of the total energy consumption via their (co-)combustions (Hu et al., 2019). The mono-combustion characteristics of TDS and sewage sludge were improved with the addition of microalgae (Peng et al., 2015), rice husk, or wood sawdust (Wang et al., 2019b). Another promising biofeedstock to enhance the co-combustion performance of TDS is waste tea (WT) owing to its high volatiles and calorific value (Cai et al., 2018). On average, 2.27 million tons of teas are harvested annually in China more than 90% of which turns into WT after its consumption. Hence, it is of great importance to explore the co-combustion applicability of WT and TDS.

* Corresponding author.

E-mail address: Liujiy@gdut.edu.cn (J. Liu).

Thermogravimetric (TG) analysis has been commonly utilized to estimate the decomposition behavior of solid materials (Chen et al., 2017a). The kinetic parameters of the thermal decomposition are estimated from TG data-derived models including iso-conversional and model-fitting ones (Yuan et al., 2017). For example, Flynn-Wall-Ozawa (FWO), and Kissinger-Akahira-Sunose (KAS) as the most common iso-conversional models (Gao et al., 2016) were used to determine the kinetics of waste-extruded polystyrene and rigid polyurethane (Jiang et al., 2018). The master-plots method as the model-fitting approach is adopted to understand the mechanisms according to the best-fit kinetic models instead of the kinetic parameter estimations (He and Ma, 2015). For example, the thermal decomposition of petrochemical wastewater sludge was characterized by three stages using the master-plots method (Chen et al., 2015b). TG coupled with mass spectrometry (TG-MS) analysis also provides the real-time detection of emissions (Wang et al., 2019b). For example, the evolved gases of the microalgae combustion were detected as NO, H₂S, COS, SO₂, and SO₃ (Fang et al., 2019). The emission characteristics of HCl and SO₂ were evaluated during the co-combustion of sub-bituminous coal and biomass (Rodilla et al., 2018). Since the high S and N concentrations of TDS and WT may produce gas pollutants during their (co-)combustions, it is necessary to monitor and quantify their kinetics and gas evolutions.

The ash depositions of the TDS (co-)combustions were found to result in corrosion and agglomeration for incinerators due to their high contents of alkali metal salts, and inorganic minerals (Wei et al., 2016). Influences of the composition, fusion temperature, and mineral distribution of ashes on their deposition can be quantified using scanning electron microscopy (SEM), X-ray diffraction (XRD) (Tang et al., 2016) and Fourier transform infrared (FTIR) (Tang et al., 2016). For example, the co-combustion of sewage sludge and lignite was shown to alter the sintering and fusion degree of their ashes through SEM and XRD analyses (Chen et al., 2015a). Similarly, the ash inorganics were detected for the co-combustion of wheat straw and sewage sludge (Wang et al., 2019a). The particle agglomeration was found to rise at fouling temperatures with the addition of sewage sludge and woody biomass to coal (Namkung et al., 2018). However, there exists no study in related literature about the ash characteristics of the co-combustion of TDS and WT in order to guide its practical applications.

The objectives of this experimental study were to quantify the behaviors, kinetics, ash components, and gas evolutions of the TDS and WT (co-)combustions. The (co-)combustion behaviors were analyzed using TG data and principal component analysis (PCA). The kinetics and mechanism functions were estimated using the FWO, KAS and master-plots methods. The ash morphology and components were detected using SEM, FTIR, BET and XRD analyses and simulated using the thermodynamic software of FactSage 7.1. The emissions were identified using TG-MS analyses.

2. Materials and methods

2.1. Sample preparations

TDS samples were gathered from a sewage treatment plant in the city of Foshan in the province of Guangdong, China. WT was sampled from tea leaves soaked for 8 h. The samples were dried in an oven at 105 °C for 24 h, pulverized using a disintegrator and sieved into particles of a 74-μm diameter. WT was blended with TDS at the ratios of 0, 10, 20, 30, 40, 50 and 100% coded as 10TDS, 90TDS10WT, 80TDS20WT, 70TDS30WT, 60TDS40WT, 50TDS50WT, and 100WT, respectively. An energy dispersive X-ray fluorescence spectrometer (XRF) (EDX7000, SHIMADZU, Japan) was utilized to characterize the bottom slag components. The fuel characteristics

and ash chemical compositions of TDS and WT are provided in Table 1.

2.2. Thermogravimetric analyses

A TG analyzer (NETZSCH STA 409 PC Luxx, Germany) was utilized to conduct TG analysis. All the samples were heated from 30 to 1000 °C in the 21% N₂ and 79% O₂ atmosphere (held constant at 60 mL/min) at 5, 10, 20 and 40 °C/min. To ensure the comparability of the (co-)combustion parameters, the samples were maintained at the same weight (6 ± 0.5 mg) in each experiment. The experiments were repeated in triplicates to keep the experimental errors within a margin of error of ±2%.

2.3. (Co-)combustion parameters

For a better understanding of the (co-)combustion properties, the (co-)combustion parameters of ignition temperature (T_i , °C), burnout temperature (T_b , °C), maximum weight loss rate ($-R_p$, %/min), peak temperature (T_p , °C), and average weight loss rate ($-R_v$, %/min) were adopted in this study. The (co-)combustion performances were also evaluated using comprehensive combustibility index (CCI) as follows (Chen et al., 2017b):

$$CCI = \frac{(-R_p) \times (-R_v)}{T_i^2 \times T_b} \quad (1)$$

where T_i is the intersection of the horizontal line of the TG curve and the tangent line of the derivative TG (DTG) curve; and T_b is the temperature with 98% weight loss.

2.4. Principal component analysis (PCA)

PCA was used to reduce the data dimensionality and to determine the predominant reactions for the (D)TG experiments with all the blend ratios (Ma et al., 2014). Upon the standardization of the variables using the descriptive function, the varimax with kaiser normalization was selected as the rotation method. The extraction method was set to principal components with a factor value of 2.

Table 1
Fuel characteristics and ash chemical components of TDS and WT.

Sample	TDS	WT (Cai et al., 2019)
Ultimate analysis (wt %)		
C	16.72 ± 0.04	47.99 ± 0.04
H	3.27 ± 0.06	6.60 ± 0.04
N	0.89 ± 0.04	4.90 ± 0.10
O	8.41 ± 0.02	28.73 ± 0.07
S	3.17 ± 0.07	0.18 ± 0.02
Proximate analysis (wt %)		
Water content	4.01 ± 0.02	5.45 ± 0.03
Volatile matter	26.14 ± 0.14	82.31 ± 0.04
Ash	63.53 ± 0.05	6.15 ± 0.06
Fix carbon	6.32 ± 0.17	6.09 ± 0.07
High heating values (MJ/kg)	3.76 ± 0.11	20.86 ± 0.03
Chemical component in ash (wt %)		
Na ₂ O	7.49	1.26
MgO	1.47	8.63
Al ₂ O ₃	0.99	4.23
SiO ₂	6.17	2.14
P ₂ O ₅	2.34	25.60
SO ₃	14.50	7.73
K ₂ O	0.26	5.04
CaO	14.52	36.55
Fe ₂ O ₃	46.28	1.18
Other	5.98	7.64

The statistical analysis was performed using SPSS 19.0.

2.5. Kinetic analysis

The (co-)combustions of TDS and WT are a very complex process due to their chemical compositions. Their kinetic parameters can be computed from the iso-conversional method without the consideration of the involved reaction mechanisms. The thermal decomposition was described as follows (Giwa et al., 2018):

$$\frac{d\alpha}{dt} = k(T)f(\alpha) \tag{2}$$

$$k(T) = A \exp(-E_a/RT) \tag{3}$$

where α , $k(T)$, t , T , A , E_a , R , and $f(\alpha)$ are the conversion degree, rate constant, reaction time (min), absolute temperature (K), pre-exponential factor (s^{-1}), apparent activation energy (kJ/mol), gas constant (8.314 J/(mol·K)), and reaction mechanism function, respectively. α can be expressed thus:

$$\alpha = (m_0 - m_t) / (m_0 - m_f) \tag{4}$$

where m_0 , m_t , and m_f are the beginning, instantaneous and final masses, respectively.

For the non-isothermal experiments, $\beta = dT/dt$ can be expressed by combining Eqs. (2) and (3) thus:

$$\frac{d\alpha}{dT} = \frac{A}{\beta} \exp\left(-\frac{E_a}{RT}\right) f(\alpha) \tag{5}$$

The integral form of Eq. (5) can be obtained as follows:

$$g(\alpha) = \int_0^\alpha \frac{d\alpha}{f(\alpha)} = \frac{A}{\beta} \int_0^T \exp\left(-\frac{E_a}{RT}\right) dT \tag{6}$$

2.5.1. Iso-conversional method

Recently, the iso-conversional methods have been widely applied to estimate E_a without having to assume the reaction model (Zhao et al., 2019). In this study, E_a estimates of the (co-)combustions were derived from the FWO and KAS methods, and Eq. (6) was re-arranged thus (Minh Loy et al., 2018):

$$\text{FWO: } \ln\beta = \ln\left(\frac{AE_a}{Rg(\alpha)}\right) - 5.3305 - 1.052\left(\frac{E_a}{RT}\right) \tag{7}$$

$$\text{KAS: } \ln\left(\frac{\beta}{T^2}\right) = \ln\left(\frac{AE_a}{Rg(\alpha)}\right) - \frac{E_a}{RT} \tag{8}$$

For a given α , E_a was estimated from the slope of the plot of $\ln(\beta)$ and $\ln(\beta/T^2)$ versus $1/T$.

2.5.2. Master-plots method

The master-plots method serves to estimate the reaction mechanisms during the single-step process (Chen et al., 2015b). When reactions were quite slow at ambient temperature (T_0), the following transformations for Eq. (6) can be obtained:

$$g(\alpha) = \frac{AE_a}{\beta R} p(u) \tag{9}$$

$$p(u) = \int_\infty^u -\left(\frac{e^{-u}}{u^2}\right) du \tag{10}$$

where $u = E_a/RT$. Since $p(u)$ has no analytical solution, the approximation yields sufficiently accurate results as follows (Cai et al., 2019):

$$P(u) = \frac{\exp(-u)}{u \times (1.00198882u + 1.87391198)} \tag{11}$$

The decomposition kinetic model with a constant $g(\alpha)$ can be based on the master-plots method. E_a and A are held constant in this single-step process. Adopting the reference at $\alpha = 0.5$, Eq. (9) can be expressed as follows (He and Ma, 2015):

$$g(0.5) = \frac{AE_a}{\beta R} p(u_{0.5}) \tag{12}$$

where $g(0.5)$ and $T_{0.5}$ represent the integral reaction model, and temperature, respectively. $u_{0.5} = E_a/RT_{0.5}$. Eqs. (9) and (12) can be re-arranged thus:

$$\frac{g(\alpha)}{g(0.5)} = \frac{p(u)}{p(u_{0.5})} \tag{13}$$

In order to capture the most possible model, the theoretical $g(\alpha)/g(0.5)$ versus α values were plotted using the 13 model

Table 2
Common mechanisms of solid state reactions (He and Ma, 2015).

Mechanisms	Symbol	$f(\alpha)$	$G(\alpha)$
Order of reaction			
First-order	F1	$1-\alpha$	$-\ln(1-\alpha)$
Second-order	F2	$(1-\alpha)^2$	$(1-\alpha)^{-1}-1$
Third-order	F3	$(1-\alpha)^3$	$[(1-\alpha)^{-2}-1]/2$
Fourth order	F4	$(1-\alpha)^4$	$[(1-\alpha)^{-3}-1]/3$
Diffusion			
One-way transport	D1	$1/(2\alpha)$	α^2
Two-way transport	D2	$[-\ln(1-\alpha)]-1$	$(1-\alpha)\ln(1-\alpha)+\alpha$
Three-way transport	D3	$(3/2)(1-\alpha)^{2/3}[1-(1-\alpha)^{1/3}]^{-1}$	$[1-(1-\alpha)^{1/3}]^2$
Ginstling–Brounshtein equation	D4	$(3/2)[(1-\alpha)^{-1/3}-1]^{-1}$	$(1-2\alpha/3)-(1-\alpha)^{2/3}$
Random nucleation and nuclei growth			
Two-dimensional	A2		$2(1-\alpha)[- \ln(1-\alpha)]^{1/2}$
Three-dimensional	A3		$3(1-\alpha)[- \ln(1-\alpha)]^{2/3}$
Limiting surface reaction between both phases			
One dimension	R1	1	α
Two dimensions	R2	$2(1-\alpha)^{1/2}$	$1-(1-\alpha)^{1/2}$
Three dimensions	R3	$3(1-\alpha)^{2/3}$	$1-(1-\alpha)^{1/3}$

functions in Table 2, while the $p(u)/p(u_{0.5})$ versus α plot was based on the experimental data. When both sides of Eq. (13) were compared, the values of $p(u)/p(u_{0.5})$ and $g(\alpha)/g(0.5)$ were equal, or in close agreement for a given α . On the contrary, a significant deviation of master-plots occurs when an inappropriate $g(\alpha)$ kinetic model is used.

2.6. Ash characteristic analysis

The ash surface and morphology following the (co-)combustions were identified using SEM (ZEISS Sigma HD, Germany). XRD (D/MAX-Ultima IV, Rigaku Corporation, Japan) was used to analyze the mineral crystalline compositions. The scans ranged from 5 to 80° at 5°/min. FTIR analysis of ash was conducted using the KBr pellet method on Nicolet IS50 spectroscopy. N₂ adsorption/desorption was measured using a surface area analyzer (ASAP 2460, Micrometrics) through Brunauer–Emmett–Teller (BET) measurements.

2.7. FactSage simulations

The FactSage 7.1 software was utilized to simulate the thermodynamic equilibria of the mineral phases. In so doing, the databases of FToxid, FTsalt and FactPS were selected. C, H, N, O, S, Na₂O, CaO, Fe₂O₃, SiO₂, P₂O₅, SO₃, K₂O, MgO, and Al₂O₃ were chosen for the reactions (Table 1). The reactions took place at 101.325 kPa pressure with the excess air ratio of 1.5. The temperature ranged from 600 to 1200 °C with a step of 50 °C.

2.8. TG-MS analyses

The gaseous products evolved from the (co-)combustions were monitored using TG-MS analyses (Rigaky-Tokyo, Japan). About 6 ± 0.5 mg of the samples were heated from 30 to 1000 °C at 10 °C/min. To avoid the effects of NO_x, the 79% He/21% O₂ atmosphere was used instead of 79% N₂/21% O₂. This study focused on the main products of NH₃, HCN, NO, CO₂, NO₂, and SO₂ with the m/z values of 17, 27, 30, 44, 46, and 64, respectively.

3. Results and discussion

3.1. Effect of blend ratio on (co-)combustions

The TG characteristics of the (co-)combustions of TDS and WT were quantified in response to 5, 10, 20, and 40 °C/min. The D(TG) curves of all the samples at 10 °C/min are presented in Fig. 1. The

TDS combustion consisted of three stages at the low temperature and had a lower peak of mass loss in the range of 830–1000 °C. TDS mainly contained dyestuff, slurry, dyeing agent, fiber, and inorganic compounds (Peng et al., 2015). The first and second stages showed the releases of moisture and some light volatiles, respectively, thus generating two small humps from 30 to 220 °C. The second stage of the TDS combustion appeared to correspond to the degradation of lipids which was highly reactive in the range of 150–240 °C (Lin et al., 2016). The third stage (devolatilization) from 220 to 650 °C mainly resulted from the degradation of macromolecule organic matter (fiber, protein, and saturated aliphatic chains). A remarkable peak (220–347 °C) was observed as the main loss one and attributed to the combustion and release of volatiles and biodegradable small-molecule organic compounds. The maximum reaction rate was achieved at 283.2 °C. The range of 347–625 °C corresponded to the high-boiling point of volatiles, refractory organic residues, fixed carbon, and active decomposition of proteins (Xie et al., 2018). The final stage between 830 and 1000 °C was attributed to the inorganic mineral decomposition. Cai et al. (2018) reported that the WT combustion consisted of the following three stages: (I) moisture removal (<185 °C), (II) devolatilization (185–604 °C) such as the combustion of (hemi)celluloses, lignin, and fixed carbon, and (III) inorganic decomposition (604 °C until the end).

As shown in Table 3, the initial temperature increased from 141.3 to 145.5 °C, while the final temperature dropped from 994.8 to 948.1 °C when WT was increased from 0 to 50%. With the increased blend ratio, the maximum peak rose to a higher temperature. This may be due to the increase in the macromolecular refractory organic compounds that made the decomposition more difficult (Chen et al., 2015a). The mass loss of the main stage rose from 36.66 to 63.41%. Also, the sharp peaks of the DTG curves with the increased WT suggested that the decomposition of more WT increased the devolatilization rate. Therefore, the WT addition appeared to avoid the drawbacks of the individual fuels and to enhance their co-combustion efficiency.

3.2. PCA analysis

PCA was used to reduce the data dimensionality and to determine the predominant reactions as well as the similarities and differences among the blend ratios (Xie et al., 2018). The two principal components extracted accounted for 52.9 (PC1) and 46.7% (PC2) (Fig. 2a), respectively, when the rotation converged for three times. The sums of squared loadings of PC1 and PC2 were 99.6%, beyond a typical threshold of 80%. The WT and TDS combustions corresponded to PC1 and PC2, respectively. The score points

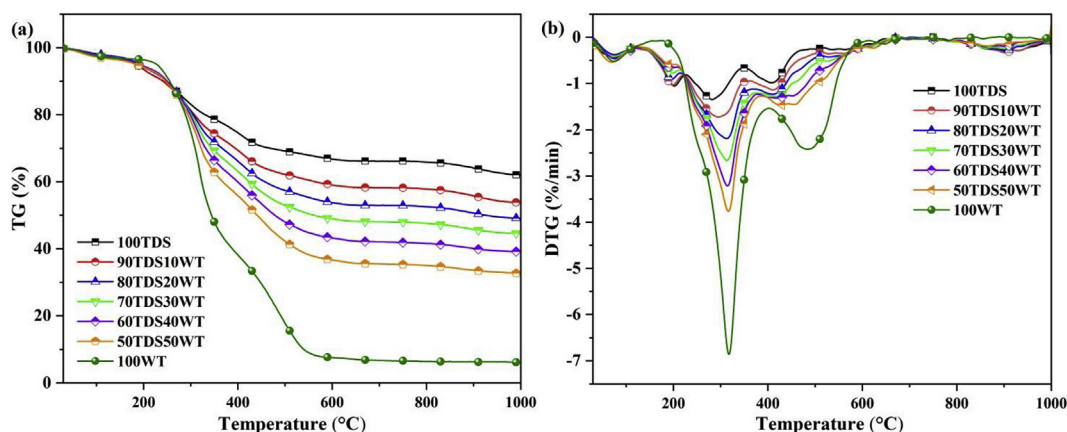


Fig. 1. (a) TG and (b) DTG curves of TDS, WT, and their blends at 10 °C/min.

Table 3
Thermal decomposition parameters of TDS, WT, and their blends at 10 °C/min.

Sample	Initial temperature (°C)	Final temperature (°C)	Maximum peak temperature (°C)	Main stage of mass loss (%)	Residue mass (%)
100TDS	141.3	994.8	283.2	36.66	62.03
90TDS10WT	141.8	990.3	295.6	43.05	53.80
80TDS20WT	142.1	983.5	309.3	48.21	49.13
70TDS30WT	142.6	973.7	314.6	52.42	44.56
60TDS40WT	143.2	961.4	316.8	57.68	39.24
50TDS50WT	145.5	948.1	317.7	63.41	33.02
100WT	178.4	612.6	320.2	88.92	6.17

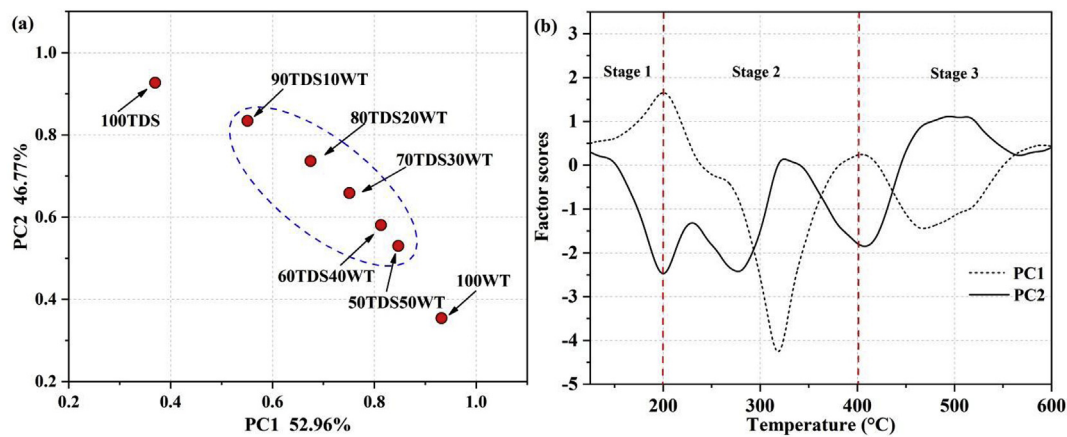


Fig. 2. (a) PCA score plot; and (b) PC1 and PC2 factor scores.

initially showed a large deviation due to the WT addition which in turn decreased gradually. This indicates that WT played a more important role in the blends due to its higher content of volatiles, while TDS exerted a lower influence on the co-combustion due to its higher ash content. The relationship between the factor scores of PC1 and PC2 and the temperature showed that the thermodynamic mode of each component can be applied to determine the predominant reactions of the co-combustion (Ma et al., 2014). The mass loss peaks of PC2 influenced all the stages, while PC1 contributed to the second and third stages (Fig. 2b). The first stage (130–200 °C) corresponded to the release of small molecular substances from TDS (PC2). The second stage was marked by the decomposition of the macromolecule organics of (hemi)celluloses, lignin, and protein. The third stage (400–600 °C) was mainly due to the decomposition of recalcitrant volatiles, and the fixed carbon combustion.

3.3. (Co-)combustion performances

To evaluate the (co-)combustion performances, the estimated (co-)combustion parameters are presented in Table 4. The decrease in T_b from 948.7 to 871.1 °C with the increased WT pointed to a lower temperature and energy requirement to complete the

combustion process. Also, T_i , T_p , $-R_p$, $-R_v$, and CCI increased. Thus, the co-combustion improved the combustion characteristic parameters. The CCI value was significantly higher for WT than TDS due to the higher volatiles content of WT. The higher CCI value represented an easier combustion reaction (Fang et al., 2015). Therefore, the increased WT resulted in the higher reactivity and a better combustion performance. Similar co-combustion results were reported for oil shale, municipal solid waste (Fan et al., 2016), coal, composite biomass (Guo and Zhong, 2018a), refinery sludge, and lignite (Chen et al., 2015a). Overall, all the parameters of the blends indicated that the combustion performance of TDS was promoted by the WT addition.

3.4. Kinetic analysis

The energy barrier of the reaction needs to be overcome during the decomposition process (Zhao et al., 2019). To investigate the reaction barrier and co-combustion mechanism, the E_a values of the blends were estimated for the main stage from 130 to 650 °C through FWO and KAS. The E_a values of the blends were similar for both methods (Fig. 3). The E_a values of TDS ranged from 115.33 to 203.64 kJ/mol (FWO) and 113.49–205.01 kJ/mol (KAS) when $\alpha \leq 0.35$. The E_a values at a low α value for TDS may be due to the

Table 4
Combustion parameters of TDS, WT, and their blends at 10 °C/min.

Sample	T_i (°C)	T_b (°C)	T_p (°C)	$-R_p$ (%/min)	$-R_v$ (%/min)	CCI ($10^{-8}\% \text{ min}^{-2} \text{ } ^\circ\text{C}^{-3}$)
100TDS	205.5	948.7	283.2	1.32	0.3998	1.32
90TDS10WT	212.2	936.3	295.6	1.71	0.4851	1.97
80TDS20WT	228.3	919.5	309.3	2.19	0.5337	2.46
70TDS30WT	246.8	906.7	314.6	2.66	0.5808	2.82
60TDS40WT	252.6	887.4	316.8	3.21	0.6383	3.64
50TDS50WT	257.5	871.1	317.7	3.77	0.7014	4.60
100WT	280.1	573.2	320.2	7.66	0.9211	15.70

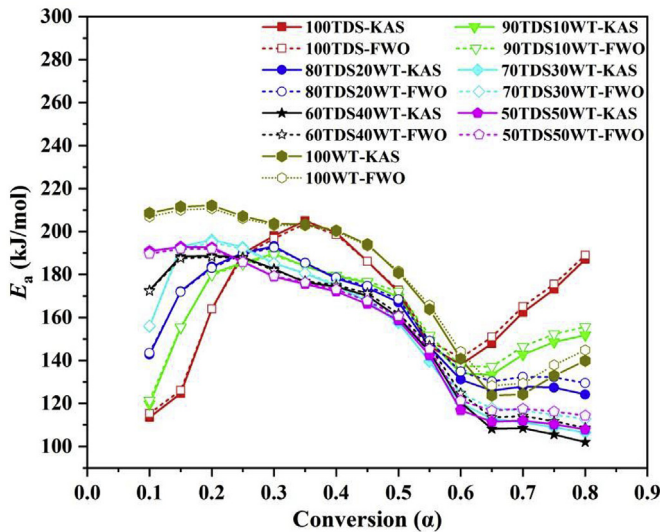


Fig. 3. E_a estimates of TDS, WT, and their blends at different values of α

decomposition of carbohydrates and lipids whose chemical bonds have poor thermal stability (Cao et al., 2016). With the temperature rise, protein and macromolecular organic matter with high thermal stability needed more E_a to break their bonds. After the α range of 0.35–0.60, the E_a values dropped from 203.15 to 141.20 kJ/mol (FWO) and 205.01 to 138.00 kJ/mol (KAS). At this stage, the degradation of volatiles formed a porous carbon structure, which provided the conditions for the oxygen diffusion to promote the combustion process (Huang et al., 2019). Then, E_a values rose again with the reaction since the organic macromolecule matter and inorganics were difficult to degrade.

According to FWO, the average E_a values of TDS and WT were 168.18 and 177.64 kJ/mol, respectively (Table 5). However, the average E_a varied with the different blend ratios considerably, thus suggesting that the co-combustion affected the thermal reaction. With the increased WT, the average E_a estimate showed a downward trend and reached its minimum (154.82 kJ/mol) with 40% WT. This synergistic effect of TDS and WT may be attributed to the catalysis of alkali metal ions-rich content of TDS such as K, and Na. The alkali metals (especially K) were reported to contain a significant catalytic effect on the tar-cracking (Hu et al., 2017), the weakened C–C bond, and the decreased E_a values for the degradation reactions (Xu et al., 2014). Therefore, the decline in E_a was most likely to stem from the enhancing effect of alkali and/or alkaline earth metals in TDS during the co-combustion. Our results implied that the co-combustion needed less energy than did the individual combustions due to the interaction between TDS and WT. A similar finding for the cornstalk and coal co-combustion was also reported by He et al. (2018). Therefore, the 60TDS40WT seemed to be the best blend ratio for their co-combustion.

Table 5
Average E_a values of TDS, WT, and their blends.

Sample	Temperature range (°C)	Average E_a by FWO (kJ/mol)	Average E_a by KAS (kJ/mol)
100TDS	144.2–645.2	168.18	167.17
90TDS10WT	143.4–646.7	161.57	159.94
80TDS20WT	145.8–642.1	159.72	157.94
70TDS30WT	142.6–647.5	155.57	153.49
60TDS40WT	145.3–650.5	154.82	152.66
50TDS50WT	143.5–653.5	156.52	154.33
100WT	185.0–604.3	177.64	176.48

The quantification of kinetic parameters facilitates the numerical simulation, design, and optimization of operational conditions to ensure the success of the thermal decomposition process (Chen et al., 2018a). To further understand the reaction mechanism at each stage, the master-plots method was adopted to explore the reaction models for the different temperature ranges. The plots of $g(\alpha)/g(0.5)$ versus α for the 13 reaction models are illustrated in Fig. 4. The $p(\mu)/p(0.5)$ (experimental) and $g(\alpha)/g(0.5)$ (theoretical) curves of the different temperature ranges were compared for TDS, WT, and 60TDS40WT at 10 °C/min. The certain models fitted most experimental results well, whereas the experimental curves of 60TDS40WT (stage 3) and WT (stage 1) did not superimpose the theoretical curves. To obtain a relatively optimal n value, $[[1-\alpha]^{1-n}-1]/(n-1)$ was compared to $E_a P(u)/\beta R$ via a linear regression line whose intercept and slope were used to determine n and A , respectively.

The kinetic parameters of n , A , and $f(\alpha)$, and the best-fit reaction models are shown for TDS, WT, and 60TDS40WT in Table 6. With the WT addition, the kinetic parameters showed different performances. In the first stage, the reaction model of TDS and 60TDS40WT was the same because WT did not begin to decompose and had no significant effect on the reaction. Likewise, the second phase appeared to have no effect on the reaction model but reduced E_a . The lower E_a values of the co-combustion may be due to the interaction between TDS and WT which is further discussed in the next section. Nevertheless, the kinetic parameters of 60TDS40WT, which corresponded to the reaction model of F2.3 ($f(\alpha) = (1-\alpha)^{2.3}$), varied greatly during the carbon combustion (third stage). This was mainly due to the decomposition of the fixed carbon combustion that improved the combustion process with the WT addition. Due to their different compositions, the thermal behavior of 60TDS40WT differed significantly from that of TDS or WT. A similar phenomenon was found for the reaction mechanism of the coal and cornstalks co-combustion (He et al., 2018).

3.5. Interaction between TDS and WT

To explore the existence of an interaction (synergistic or inhibitive) between TDS and WT, their theoretical values were compared to the weighted average of the individual fuels. In the case of no interaction, the co-combustion characteristics were assumed to follow a weighted average of the individual fuels (Chen et al., 2015a). The estimated TG (TG_{Cal}) values of the blends were defined as follows (Chen et al., 2018b):

$$TG_{Cal} = \alpha_{TDS}TG_{TDS} + \alpha_{WT}TG_{WT} \quad (14)$$

$$Deviation (\%) = (TG_{Exp} - TG_{Cal})/TG_{Cal} \quad (15)$$

$$DTG_{Cal} = \alpha_{TDS}DTG_{TDS} + \alpha_{WT}DTG_{WT} \quad (16)$$

where $(D)TG_{Exp}$ and $(D)TG_{Cal}$ were the experimental and calculated curves, while α_{TDS} and α_{WT} were the mass ratios of TDS and WT,

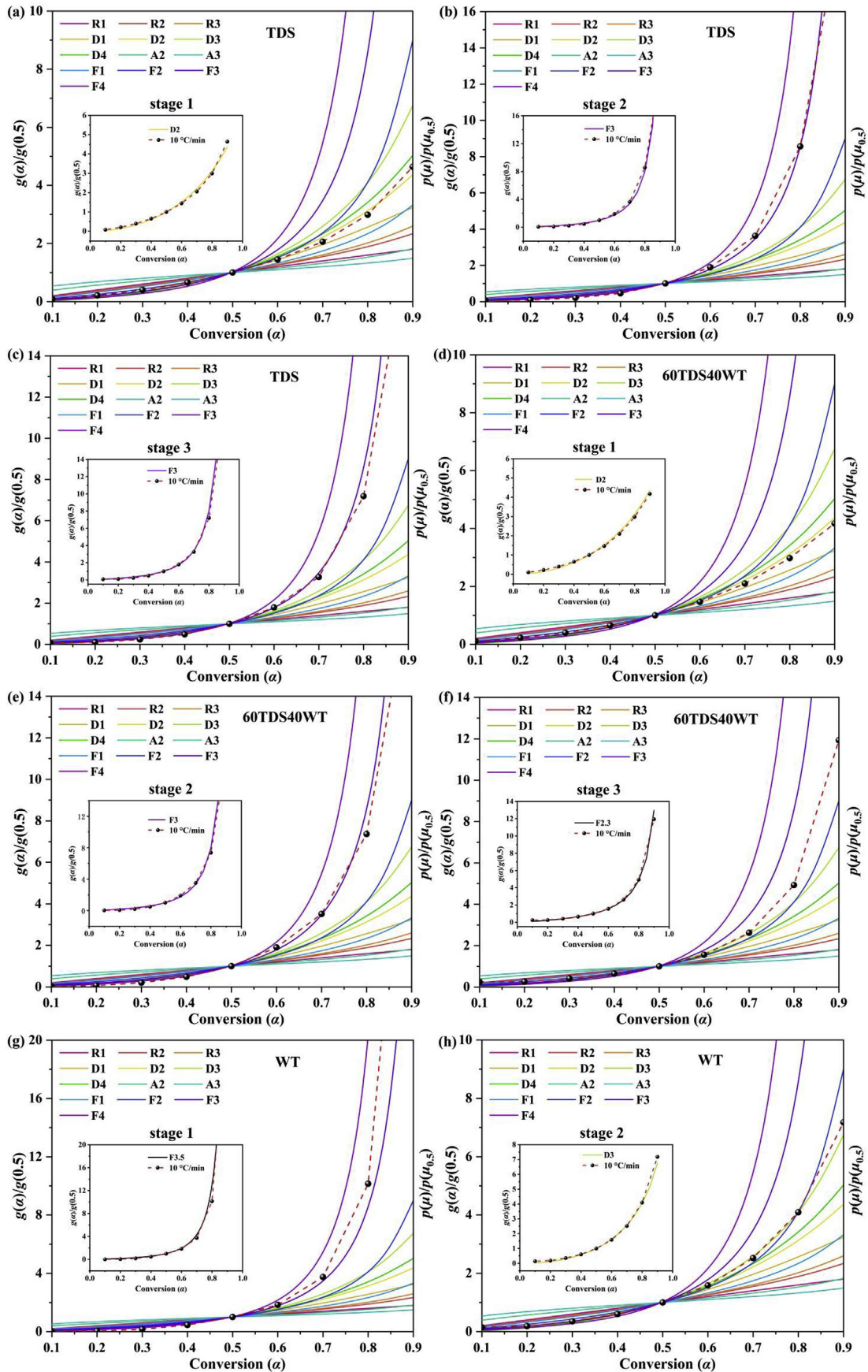


Fig. 4. Theoretical curves of $g(\alpha)/g(0.5)$ versus α for 13 reaction models, and experimental curves of $p(u)/p(u_{0.5})$ versus conversion degree for experimental data for (a, b, c) TDS, (d, e, f) 60TDS/40WT, and (g, h) WT.

Table 6
Kinetic parameters of thermal degradation of different temperature ranges for TDS, 60TDS40WT, and WT at 10 °C/min.

Sample	Temperature range (°C)	Average E_a (kJ/mol)	A (s^{-1})	Model	$f(\alpha)$
TDS	144.3–227.5	119.05	1.78×10^{13}	D2	$[-\ln(1 - \alpha)]^{-1}$
	227.5–351.2	182.63	2.18×10^{17}	F3	$(1 - \alpha)^3$
	351.2–645.8	167.60	5.91×10^{12}	F3	$(1 - \alpha)^3$
60TDS40WT	145.7–645.8	127.00	2.40×10^{14}	D2	$[-\ln(1 - \alpha)]^{-1}$
	209.3–377.4	169.61	1.28×10^{15}	F3	$(1 - \alpha)^3$
	377.4–654.5	106.53	6.04×10^7	F2.3	$(1 - \alpha)^{2.3}$
WT	187.3–400.4	214.03	1.20×10^{19}	F3.5	$(1 - \alpha)^{3.5}$
	400.4–604.1	165.58	1.47×10^{11}	D3	$(3/2)(1 - \alpha)^{2/3}[1 - (1 - \alpha)^{1/3}]^{-1}$

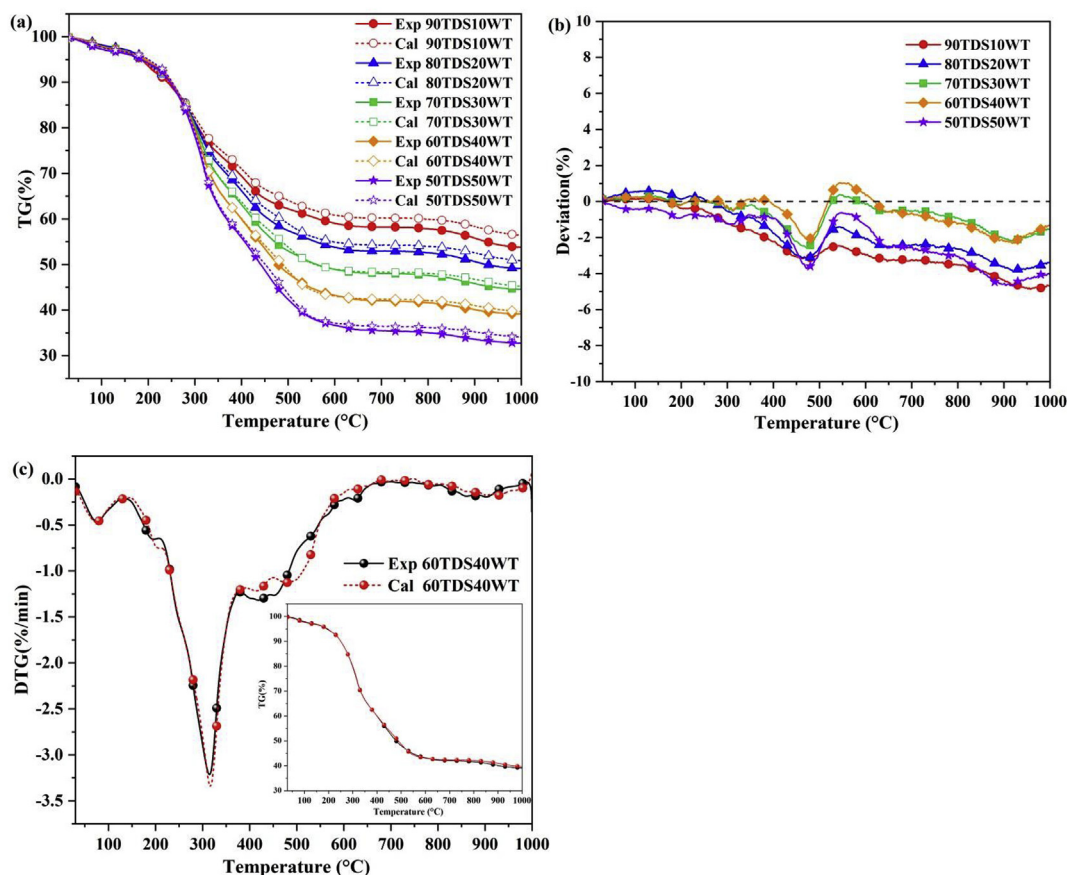


Fig. 5. (a) TG curves of calculated and experimental; (b) deviation curves of five blends; and (c) (D)TG curves of 60TDS40WT.

respectively.

The experimental TG curves staying mostly below the calculated ones showed that the experimental residue mass was less than the estimated one for the blends (Fig. 5a). This indicated the interaction between TDS and WT which boosted their decomposition. Fig. 5b shows the deviation curves of the co-combustion with the increased temperature. A positive deviation value (%) shows the inhibition of the combustion reaction, while a negative value means the promoted reaction process (Peng et al., 2015). The negative deviation of the five blends indicated the enhanced combustion process. The deviation curves of all the blends reached the peaks at 480 and 550 °C where the interaction peaked.

The consistency of the measured and predicted curves of 60TDS40WT during the stages of evaporation, and the volatiles combustion at below 370 °C indicated no interaction between TDS and WT (Fig. 5c). However, the (D)TG curves distinctly differed in the range of 370–550 °C. From 370 to 470 °C, the experimental curves had a faster decomposition rate than did the predicted ones

due to the synergistic effect of TDS and WT. The relatively high volatiles content of WT generated more energy which in turn promoted the endothermic reaction to a certain extent. Thus, the TDS residues were further burned and decomposed. At the same time, the inorganic salts (silicates, carbonates, and aluminates), and a large amount of metal oxides contained by TDS appeared to catalyze the fixed carbon combustion of WT, thus accelerating the decomposition rate. Similarly, the accelerated co-combustion of municipal waste and oil shale was tied to the presence of inorganic minerals (Fan et al., 2016). The experimental (D)TG curves being above the estimated ones between 470 and 550 °C pointed to the inhibitive influence on the co-combustion. This may be attributed to the completely decomposed TDS at above 480 °C that produced a good deal of ash covering the fixed carbon surface, thus affecting the diffusion and heat transfer. At above 550 °C, the interaction was almost non-existent where the experimental and calculated (D)TG curves overlapped.

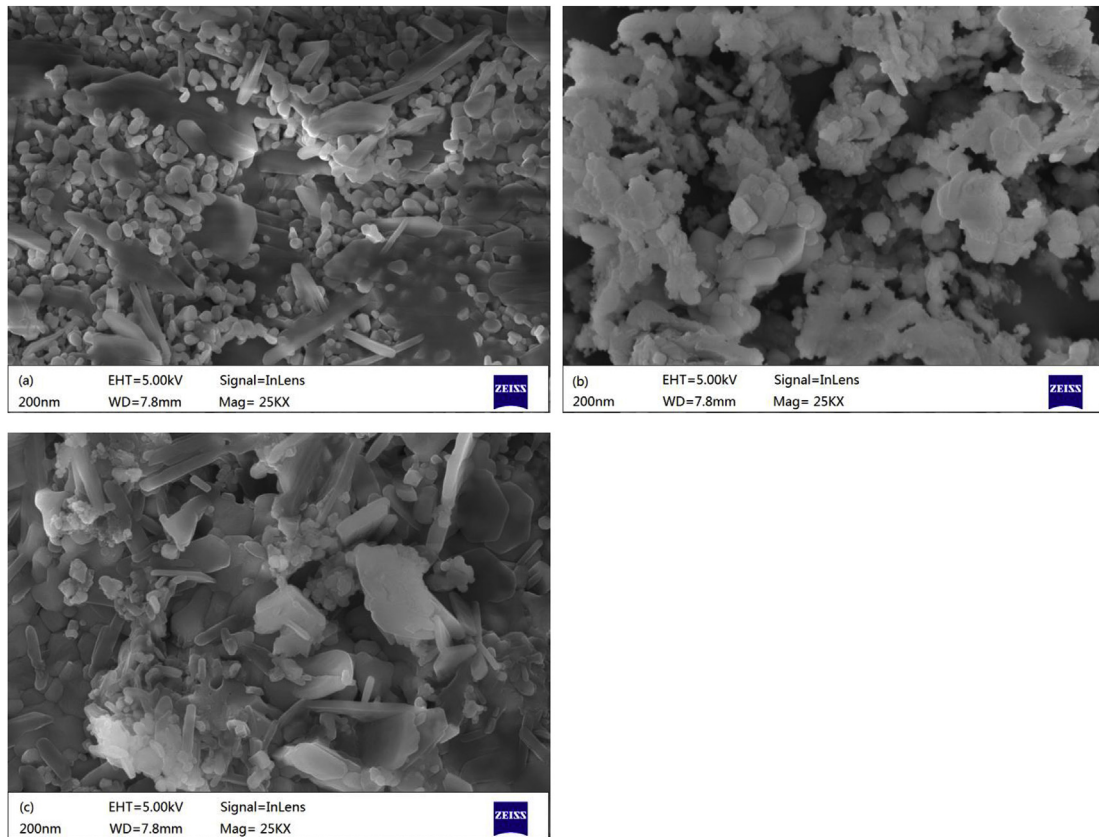


Fig. 6. SEM images of (co-)combustion ashes: (a) TDS, (b) WT, and (c) 60TDS40WT

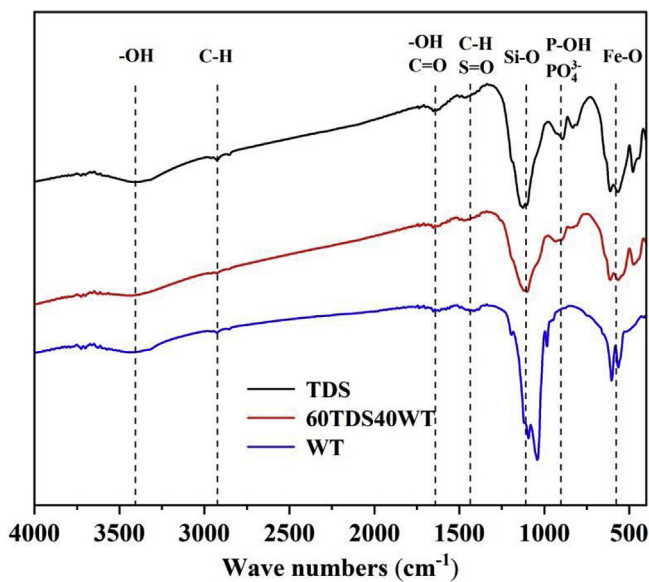


Fig. 7. FTIR spectra of ashes of TDS, WT and 60TDS40WT (co-)combustions.

3.6. Ash compositions and characteristics

3.6.1. SEM and BET

The chemical and physical properties of ashes, and their industrial utilization potential are significantly affected by their morphology (Wang et al., 2017b). The micro-morphology of the solid residues following the (co-)combustions is presented in Fig. 6.

The production of ash particles with a dense structure and smooth surface during the TDS combustion suggested that the particles experienced a significant melting and agglomeration process (Fig. 6a). This mainly resulted from the high alkali metal content of TDS that reduced the ash melting point, thus forming a low-melting point compounds (Wang et al., 2017a). The morphology of the WT solid residue with a loose, rough and pore-enriched structure is shown in Fig. 6b. Following the release of volatiles and the fixed carbon combustion, the nearly spherical ash particles appeared. The residues of lignite were reported to have a similar shape with a high specific surface area (Chen et al., 2015a). The appearance of the ash residues with the WT addition is presented in Fig. 6c. The micro-morphology evolution showed that the 60TDS40WT solid particles had a bigger, rougher, and looser structure than did the TDS ones due to the unmelted ash particles adhered to the melted minerals. Therefore, the WT addition appeared to improve the particle morphology of the bottom ash of TDS. Meanwhile, the BET surface areas of TDS, WT, and their blend were estimated at 1.77, 8.54 and 4.90 m²/g, respectively. This indicated that the WT addition improved the surface area of TDS which in turn enhanced the contact area of the combustion atmosphere and reduced the risks of fouling and agglomeration for the incinerators.

3.6.2. FTIR

The infrared spectra of the ashes of TDS, WT, and their blend are shown in Fig. 7. The absorption band between 3300 and 3500 cm⁻¹ corresponded to -OH stretching vibration in hydroxyl groups, most likely due to water, or other compounds containing -OH (Alqadami et al., 2017). The vibration bands at 2924 and 2854 cm⁻¹ may be due to the C-H stretching vibrations (Naushad et al., 2017). The absorption peak at 1653 cm⁻¹ may be related to -OH bending, and

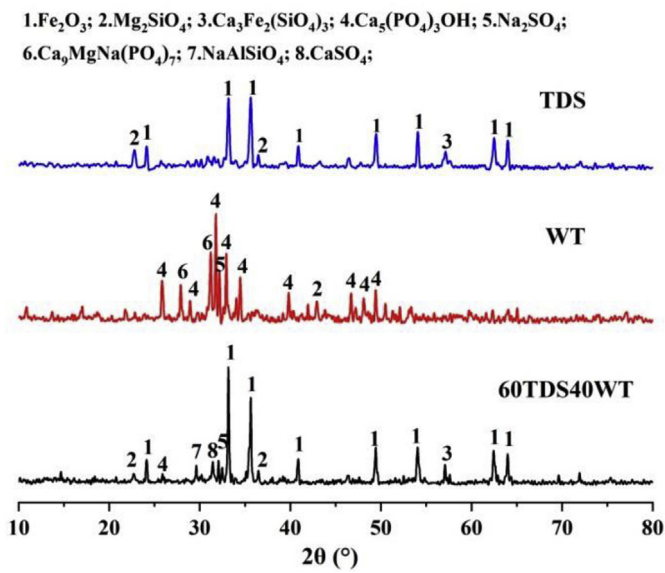


Fig. 8. XRD patterns of ashes of the (co-)combustions of TDS, WT, and 60TDS40WT

C=O stretching, indicative of water (Naushad et al., 2016), and carbonate (Liu et al., 2018). The bands at 1458 cm^{-1} and 1125 cm^{-1} may be from S=O stretching, and Si-O, respectively, thus pointing to the presence of sulfates, silicate, and SiO_2 in the ash (Gao et al.,

2017). The peaks at 1029 cm^{-1} and between 892 and 1000 cm^{-1} were related to the PO_4^{3-} and P-OH groups, respectively, due to the P content of the ash (El-Nahas et al., 2017). The band between 550 and 620 cm^{-1} was due to the Fe-O bond (Alqadami et al., 2016). According to our FTIR results, the ash mainly contained inorganic compounds.

3.6.3. XRD analysis

To further illustrate the morphology and composition of minerals, XRD was used to analyze the residual ashes of TDS, WT, and their blend. As shown in Fig. 8, Fe_2O_3 , Mg_2SiO_4 , and $\text{Ca}_3\text{Fe}_2(\text{SiO}_4)_3$ were the main mineral compositions of the TDS ash. The transformation pathways may follow the following equations: $2\text{MgO} + \text{SiO}_2 = \text{Mg}_2\text{SiO}_4$, and $3\text{CaO} + \text{Fe}_2\text{O}_3 + 3\text{SiO}_2 = \text{Ca}_3\text{Fe}_2(\text{SiO}_4)_3$. The peak intensity of Fe_2O_3 was most intense, whereas the intensities of Ca and Mg were relatively low according to our XRF results in Table 1. Meanwhile, Fe_2O_3 was very difficult to decompose at below 1000°C , and thus, existed in a large amount in the bottom ash (Sun et al., 2019). The residue composition of WT mainly included $\text{Ca}_5(\text{PO}_4)_3\text{OH}$, Mg_2SiO_4 , Na_2SO_4 , and $\text{Ca}_9\text{MgNa}(\text{PO}_4)_7$ due to the large amounts of Ca, Mg, and P in WT. The WT addition changed the peak strength of Fe_2O_3 and produced the new diffraction peaks of NaAlSiO_4 and CaSO_4 . NaAlSiO_4 with the higher fusion point (1550°C) was reported to spring from the $\text{NaAlSi}_3\text{O}_8$ decomposition at 1000°C ($\text{NaAlSi}_3\text{O}_8 = \text{NaAlSiO}_4 + \text{SiO}_2$) and also via the following reaction: $\text{Na}_2\text{O} + 2\text{SiO}_2 + \text{Al}_2\text{O}_3 = 2\text{NaAlSiO}_4$ (Lu et al., 2017). NaAlSiO_4 remained in the residual ash due to its obstinacy at the high temperature. CaSO_4 may be formed by SO_2

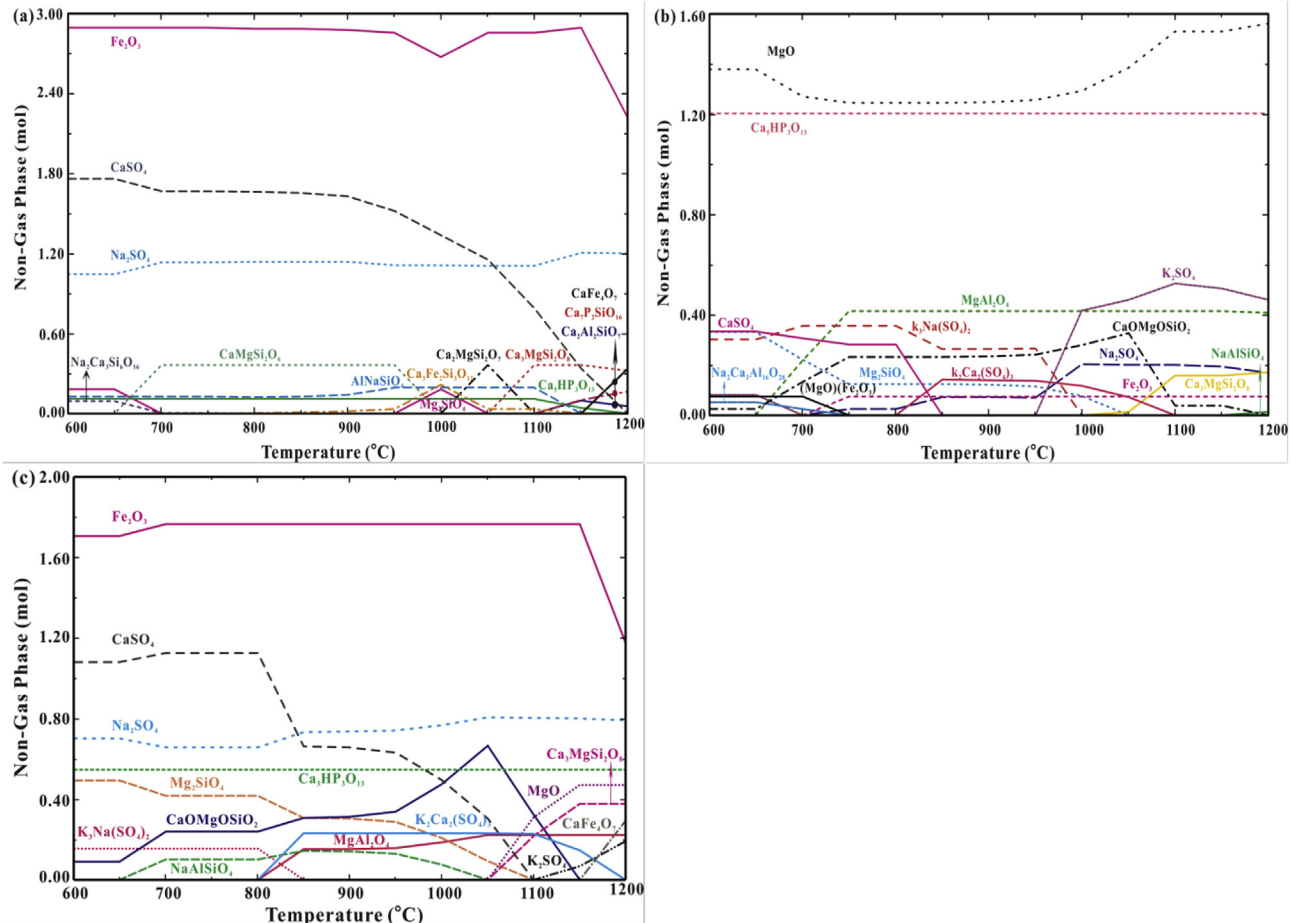


Fig. 9. Stable solid phases in equilibrium for ashes of (a) TDS, (b) WT, and (c) 60TDS40WT

absorbing CaCO_3 ($\text{CaCO}_3 + \text{SO}_2 + 1/2\text{O}_2 = \text{CaSO}_4 + \text{CO}_2$). Due to the rich S and Na contents of the blend, Na_2SO_4 was generated through gaseous or condensed Na reacting with SO_2/SO_3 (Wang et al., 2018). A large amount of Na_2O , CaO , Fe_2O_3 , and SiO_2 may cause the low melting-point compounds to form during the (co-)combustions. The agglomeration behavior was mainly caused by the formation of the eutectic compounds (Wang et al., 2017b). These findings about the changes in the composition and morphology of the ashes provide insights into how the adverse effects such as fouling, and agglomeration can be prevented or mitigated in the practical applications of the TDS and WT (co-)combustions.

3.7. Thermodynamic equilibrium simulations

The thermochemical processes of the phase evolutions as a

function of temperature can be simulated using the FactSage software (Xiang et al., 2019). The predicted major solid phases of TDS, WT, and 60TDS40WT are presented in Fig. 9. As for TDS (Fig. 9a), Fe_2O_3 was relatively stable with the increased temperature but transformed into $\text{Ca}_3\text{Fe}_2(\text{SiO}_4)_3$ between 900 and 1100 °C and CaFe_4O_7 at above 1150 °C. CaSO_4 started to decompose at above 900 °C and completely decomposed at 1200 °C, while Na_2SO_4 was stable in the ash slag. Mg_2SiO_4 was converted by the decomposition of $\text{CaMgSi}_2\text{O}_6$ with the increased temperature. The predicted slag of WT included MgO , $\text{Ca}_5\text{HP}_3\text{O}_{13}$, K_2SO_4 , MgAl_2O_4 , Na_2SO_4 , and $\text{Ca}_3\text{MgSi}_2\text{O}_8$ (Fig. 9b). Most of Mg existed mainly as MgO and Mg_2SiO_4 and was converted to MgAl_2O_4 , and $\text{CaO} \cdot \text{MgO} \cdot \text{SiO}_2$ with the increased temperature. The WT addition rendered the compositions more complicated (Fig. 9c). The transformation trend of CaSO_4 for 60TDS40WT was different from that of WT and TDS due

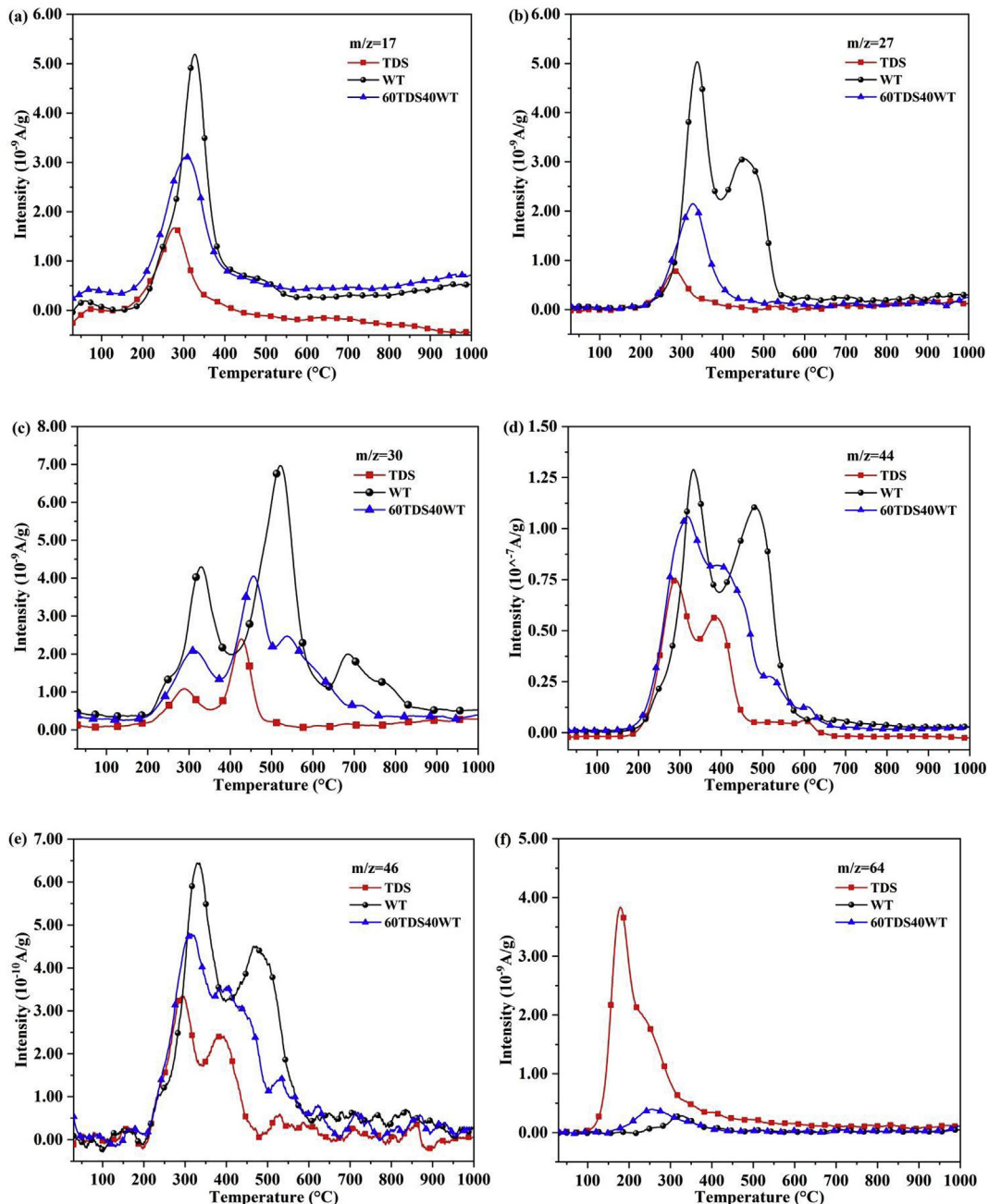


Fig. 10. Emission curves of TDS, WT, and their blend at 10 °C/min for: (a) NH_3 , (b) HCN , (c) NO , (d) CO_2 , (e) NO_2 , and (f) SO_2 .

to its combination with K to form $K_2Ca_2(SO_4)_3$ at the low temperature. The low temperature eutectic compounds formed by alkali compounds interacting with the other species (Ca, Al, and Si) lowered the ash fusion temperature and promoted the ash slagging and fouling (Yang et al., 2018). The main slagging components at 1000 °C contained Fe_2O_3 , $CaSO_4$, Na_2SO_4 , $Ca_5HP_3O_{13}$, Mg_2SiO_4 , $K_2Ca_2(SO_4)_3$, $CaO \cdot MgO \cdot SiO_2$, $MgAl_2O_4$, and $NaAlSiO_4$ which was in close agreement with our XRD results. The simulation results were used for the trend analysis and cannot replace the actual experimental tests.

3.8. TG-MS analyses

To monitor and control the release of gas pollutants to the environment from the (co-)combustions, the emission characteristics of the typical gases are presented in Fig. 10. Most gas releases had distinct trends in the range of 200–600 °C. NH_3 and HCN were considered to be the intermediate species of NO_x (Lin et al., 2017). As shown in Fig. 10a and b, the NH_3 and HCN emissions were higher from WT than TDS due to the higher N content of WT than TDS (Table 1). The N content of WT was related to crude protein, whereas that of TDS came from organics generated during the biological or stabilization treatment (Peng et al., 2015). With the increased temperature, NH_3 and HCN were generated mainly from N-containing structures with thermal instability at the lower temperature. However, an obvious peak of HCN for WT appeared in the range of 400–550 °C which may be related to the small amounts of N-containing compounds with high binding energy. With 40% WT, HCN significantly declined since the interaction reduced the HCN yield. A similar result was found by Huang et al. (2019). The release characteristics of NO_x as the main air pollutants from the TDS and WT combustions are shown in Fig. 10c and e. NO_x was produced in a small amount at lower temperatures but in a large amount from 200 to 480 °C for TDS and 200–600 °C for WT. The first release peak of NO_x was due to the decomposition of volatiles, while the latter peak resulted from the fixed carbon combustion with N-containing compounds.

Fig. 10d shows the emission pattern of CO_2 with the increased temperature. CO_2 had the maximum ion intensity as the main gas product among the others. The first release peak of TDS was mainly due to the biodegradable small-molecule organic compounds, while that of WT came from the carboxyl ($-COOH$) and $C=O$ in (hemi)celluloses. The thermolabile functional groups ($-COOH$, $C=O$) contributed to CO_2 emission when broken and reformed during the reaction (Cai et al., 2019). The second peak of the samples was attributed to the secondary decomposition of macromolecular organics, and the fixed carbon combustion. The emission strength curve of 60TDS/40WT was in between that of TDS and WT.

SO_2 emissions from the TDS and WT (co-)combustions are presented in Fig. 10f. SO_2 emission from TDS occurred mainly between 120 and 500 °C, given that organic S was the main existence modality for TDS. Organic S was previously reported to decompose at low temperatures, whereas inorganic S was released at higher temperatures (Ren et al., 2017). SO_2 emission from the WT combustion had a low intensity due to the low S content of WT. 40% WT reduced the SO_2 emission to a lower level since the high Ca content of WT reacted with SO_2 to form $CaSO_4$ ($CaCO_3 + SO_2 + 1/2O_2 = CaSO_4 + CO_2$). This finding was also confirmed by our XRD result that $CaSO_4$ intensity grew stronger with the WT addition. Overall, the WT addition appeared to inhibit the SO_2 emission from TDS, thus reducing its emission from the co-combustion. Therefore, the monitoring of the evolved gases proved to be important to the pollution control practices for the co-combustion.

4. Conclusions

In this study, the (co-)combustion performances, kinetics, gas evolutions, and ash depositions of TDS and WT were quantified. The WT addition appeared to avoid the drawbacks of the individual fuels and to enhance their co-combustion efficiency. The blends resulted in the higher reactivity and the better combustion performance. The average E_a reached its minimum (154.82 kJ/mol) with 40% WT. The best-fit reaction mechanisms of the three stages of 60TDS40WT were D2, F3, and F2.3, respectively. The interaction between TDS and WT mainly occurred between 370 and 550 °C. The WT addition caused the micro-morphology of the blend solid particles to have a bigger, rougher, and looser structure than did that of the TDS ones according to the SEM and BET surface area analyses. The WT addition changed the peak strength of Fe_2O_3 and produced the new diffraction peaks of $NaAlSiO_4$ and $CaSO_4$. The main ash compositions of the blend contained Fe_2O_3 , $CaSO_4$, Na_2SO_4 , $Ca_5HP_3O_{13}$, and $NaAlSiO_4$ according to the XRD analysis, and the thermodynamic simulations. The NH_3 , HCN, NO, CO_2 , NO_2 and SO_2 emissions mainly occurred between 200 and 600 °C. The co-combustion seemed to reduce the SO_2 emission relative to the individual combustions. Our quantification and characterization of the optimal blend ratio, the kinetic responses, the ash compositions, and the emissions can be benefited to provide insight into reduced environmental pollution, enhanced bioenergy generation, improved combustion performance, scaling-up, and optimization for the practical industrial applications of the (co-)combustions of TDS and WT.

Acknowledgments

This research was funded by the Science and Technology Planning Project of Guangdong Province (No: 2015B020235013, 2017A050501036, 2018A050506046, and 2019B020208017), the National Natural Science Foundation of China (No: 51608129), and the Science and Technology Planning Project of Shaoguan, Guangdong Province, China (No: 2019CS05307).

References

- Albadarin, A.B., Collins, M.N., Naushad, M., Shirazian, S., Walker, G., Mangwandi, C., 2017. Activated lignin-chitosan extruded blends for efficient adsorption of methylene blue. *Chem. Eng. J.* 307, 264–272.
- Alqadami, A.A., Naushad, M., Abdalla, M.A., Khan, M.R., Alothman, Z.A., 2016. Adsorptive removal of toxic dye using Fe_3O_4 -TSC nanocomposite: equilibrium, kinetic, and thermodynamic studies. *J. Chem. Eng. Data* 61 (11), 3806–3813.
- Alqadami, A.A., Naushad, M., Alothman, Z.A., Ghfar, A.A., 2017. Novel metal-organic framework (MOF) based composite material for the sequestration of U(VI) and Th(IV) metal ions from aqueous environment. *ACS Appl. Mater. Interfaces* 9 (41), 36026–36037.
- Cai, H., Liu, J., Xie, W., Kuo, J., Buyukada, M., Evrendilek, F., 2019. Pyrolytic kinetics, reaction mechanisms and products of waste tea via TG-FTIR and Py-GC/MS. *Energy Convers. Manag.* 184, 436–447.
- Cai, H., Zou, H., Liu, J., Xie, W., Kuo, J., Buyukada, M., Evrendilek, F., 2018. Thermal degradations and processes of waste tea and tea leaves via TG-FTIR: combustion performances, kinetics, thermodynamics, products and optimization. *Bioresour. Technol.* 268, 715–725.
- Cao, L., Yuan, X., Jiang, L., Li, C., Xiao, Z., Huang, Z., Chen, X., Zeng, G., Li, H., 2016. Thermogravimetric characteristics and kinetics analysis of oil cake and torrefied biomass blends. *Fuel* 175, 129–136.
- Chen, G., He, S., Cheng, Z., Guan, Y., Yan, B., Ma, W., Leung, D.Y.C., 2017a. Comparison of kinetic analysis methods in thermal decomposition of cattle manure by thermogravimetric analysis. *Bioresour. Technol.* 243, 69–77.
- Chen, J., Lang, X., Wang, Y., Li, G., Yang, Z., Fan, S., 2018a. Comparative evaluation of different non-condensable gases on thermal behaviors, kinetics, high pressure properties, and product characteristics of heavy oil. *Energy Convers. Manag.* 162, 13–25.
- Chen, J., Mu, L., Cai, J., Yin, H., Song, X., Li, A., 2015a. Thermal characteristics and kinetics of refining and chemicals wastewater, lignite and their blends during combustion. *Energy Convers. Manag.* 100, 201–211.
- Chen, J., Mu, L., Jiang, B., Yin, H., Song, X., Li, A., 2015b. TG/DSC-FTIR and Py-GC investigation on pyrolysis characteristics of petrochemical wastewater sludge.

- Bioresour. Technol. 192, 1–10.
- Chen, J., Wang, Y., Lang, X., Ren, X., Fan, S., 2017b. Comparative evaluation of thermal oxidative decomposition for oil-plant residues via thermogravimetric analysis: thermal conversion characteristics, kinetics, and thermodynamics. *Bioresour. Technol.* 243, 37–46.
- Chen, L., Yu, Z., Fang, S., Dai, M., Ma, X., 2018b. Co-pyrolysis kinetics and behaviors of kitchen waste and *Chlorella vulgaris* using thermogravimetric analyzer and fixed bed reactor. *Energy Convers. Manag.* 165, 45–52.
- Daneshvar, E., Vazirzadeh, A., Niazi, A., Kousha, M., Naushad, M., Bhatnagar, A., 2017. Desorption of Methylene blue dye from brown macroalga: effects of operating parameters, isotherm study and kinetic modeling. *J. Clean. Prod.* 152, 443–453.
- El-Nahas, A.M., Salaheldin, T.A., Zaki, T., El-Maghrabi, H.H., Marie, A.M., Morsy, S.M., Allam, N.K., 2017. Functionalized cellulose-magnetite nanocomposite catalysts for efficient biodiesel production. *Chem. Eng. J.* 322, 167–180.
- Fan, Y., Yu, Z., Fang, S., Lin, Y., Liao, Y., Ma, X., 2016. Investigation on the co-combustion of oil shale and municipal solid waste by using thermogravimetric analysis. *Energy Convers. Manag.* 117, 367–374.
- Fang, S., Yu, Z., Lin, Y., Hu, S., Liao, Y., Ma, X., 2015. Thermogravimetric analysis of the co-pyrolysis of paper sludge and municipal solid waste. *Energy Convers. Manag.* 101, 626–631.
- Fang, P., Gong, Z., Wang, Z., Wang, Z., Meng, F., 2019. Study on combustion and emission characteristics of microalgae and its extraction residue with TG-MS. *Renew. Energy* 140, 884–894.
- Gao, Y., Tahmasebi, A., Dou, J., Yu, J., 2016. Combustion characteristics and air pollutant formation during oxy-fuel co-combustion of microalgae and lignite. *Bioresour. Technol.* 207, 276–284.
- Gao, Z., Zhang, H., Ao, W., Li, J., Liu, G., Chen, X., Fu, J., Ran, C., Liu, Y., Kang, Q., Mao, X., Dai, J., 2017. Microwave pyrolysis of textile dyeing sludge in a continuously operated auger reactor: condensates and non-condensable gases. *Environ. Pollut.* 228, 331–343.
- Giwa, A.S., Xu, H., Wu, J., Li, Y., Chang, F., Zhang, X., Jin, Z., Huang, B., Wang, K., 2018. Sustainable recycling of residues from the food waste (FW) composting plant via pyrolysis: thermal characterization and kinetic studies. *J. Clean. Prod.* 180, 43–49.
- Guo, F., Zhong, Z., 2018a. Optimization of the co-combustion of coal and composite biomass pellets. *J. Clean. Prod.* 185, 399–407.
- Guo, F., Zhong, Z., 2018b. Pollution emission and heavy metal speciation from co-combustion of sedum plumbizincicola and sludge in fluidized bed. *J. Clean. Prod.* 179, 317–324.
- He, Y., Chang, C., Li, P., Han, X., Li, H., Fang, S., Chen, J., Ma, X., 2018. Thermal decomposition and kinetics of coal and fermented cornstark using thermogravimetric analysis. *Bioresour. Technol.* 259, 294–303.
- He, Y., Ma, X., 2015. Comparative investigation on non-isothermal kinetics for thermo-degradation of lignocellulosic substrate and its chlorinated derivative in atmospheres with CO₂ participation. *Bioresour. Technol.* 189, 71–80.
- Hu, J., Si, Y., Yang, H., Shao, J., Wang, X., Lei, T., Agblevor, F.A., Chen, H., 2017. Influence of volatiles-char interactions between coal and biomass on the volatiles released, resulting char structure and reactivity during co-pyrolysis. *Energy Convers. Manag.* 152, 229–238.
- Hu, J., Yan, Y., Evrendilek, F., Buyukada, M., Liu, J., 2019. Combustion behaviors of three bamboo residues: gas emission, kinetic, reaction mechanism and optimization patterns. *J. Clean. Prod.* 235, 549–561.
- Huang, J., Liu, J., Kuo, J., Xie, W., Zhang, X., Chang, K., Buyukada, M., Evrendilek, F., 2019. Kinetics, thermodynamics, gas evolution and empirical optimization of (co-)combustion performances of spent mushroom substrate and textile dyeing sludge. *Bioresour. Technol.* 280, 313–324.
- Jiang, L., Zhang, D., Li, M., He, J., Gao, Z., Zhou, Y., Sun, J., 2018. Pyrolytic behavior of waste extruded polystyrene and rigid polyurethane by multi kinetics methods and Py-GC/MS. *Fuel* 222, 11–20.
- Lin, Y., Liao, Y., Yu, Z., Fang, S., Lin, Y., Fan, Y., Peng, X., Ma, X., 2016. Co-pyrolysis kinetics of sewage sludge and oil shale thermal decomposition using TGA–FTIR analysis. *Energy Convers. Manage.* 118, 345–352.
- Lin, Y., Liao, Y., Yu, Z., Fang, S., Ma, X., 2017. A study on co-pyrolysis of bagasse and sewage sludge using TG-FTIR and Py-GC/MS. *Energy Convers. Manag.* 151, 190–198.
- Liu, Y., Ran, C., Siddiqui, A.R., Mao, X., Kang, Q., Fu, J., Deng, Z., Song, Y., Jiang, Z., Zhang, T., Dai, J., 2018. Pyrolysis of textile dyeing sludge in fluidized bed and microwave-assisted auger reactor: comparison and characterization of pyrolysis products. *J. Hazard Mater.* 359, 454–464.
- Lu, Y., Wang, Y., Xu, Y., Li, Y., Hao, W., Zhang, Y., 2017. Investigation of ash fusion characteristics and migration of sodium during co-combustion of Zhundong coal and oil shale. *Appl. Therm. Eng.* 121, 224–233.
- Ma, J., Wang, Z., Zhu, C., Xu, Y., Wu, Z., 2014. Electrogenesis reduces the combustion efficiency of sewage sludge. *Appl. Energy* 114, 283–289.
- Minh Loy, A.C., Yusup, S., Fui Chin, B.L., Wai Gan, D.K., Shahbaz, M., Acda, M.N., Unrean, P., Rianawati, E., 2018. Comparative study of in-situ catalytic pyrolysis of rice husk for syngas production: kinetics modelling and product gas analysis. *J. Clean. Prod.* 197, 1231–1243.
- Namkung, H., Lee, Y., Park, J., Song, G., Choi, J., Choi, Y., Park, S., Kim, J., 2018. Blending effect of sewage sludge and woody biomass into coal on combustion and ash agglomeration behavior. *Fuel* 225, 266–276.
- Naushad, M., Ahamad, T., Al-Maswari, B.M., Abdullah Alqadami, A., Alshehri, S.M., 2017. Nickel ferrite bearing nitrogen-doped mesoporous carbon as efficient adsorbent for the removal of highly toxic metal ion from aqueous medium. *Chem. Eng. J.* 330, 1351–1360.
- Naushad, M., Ahamad, T., Sharma, G., Al-Muhtaseb, A.a.H., Albadarin, A.B., Alam, M.M., Allothman, Z.A., Alshehri, S.M., Ghfar, A.A., 2016. Synthesis and characterization of a new starch/SnO₂ nanocomposite for efficient adsorption of toxic Hg²⁺ metal ion. *Chem. Eng. J.* 300, 306–316.
- Peng, X., Ma, X., Xu, Z., 2015. Thermogravimetric analysis of co-combustion between microalgae and textile dyeing sludge. *Bioresour. Technol.* 180, 288–295.
- Ren, X., Sun, R., Meng, X., Vorobiev, N., Schiemann, M., Levendis, Y.A., 2017. Carbon, sulfur and nitrogen oxide emissions from combustion of pulverized raw and torrefied biomass. *Fuel* 188, 310–323.
- Rodiilla, I., Contreras, M.L., Bahillo, A., 2018. Thermogravimetric and mass spectrometric (TG-MS) analysis of sub-bituminous coal-energy crops blends in N₂, air and CO₂/O₂ atmospheres. *Fuel* 215, 506–514.
- Sun, G., Zhang, G., Liu, J., Xie, W., Evrendilek, F., Buyukada, M., 2019. (Co-)combustion behaviors and products of spent potlining and textile dyeing sludge. *J. Clean. Prod.* 224, 384–395.
- Tang, Z., Chen, X., Liu, D., Zhuang, Y., Ye, M., Sheng, H., Xu, S., 2016. Experimental investigation of ash deposits on convection heating surfaces of a circulating fluidized bed municipal solid waste incinerator. *J. Environ. Sci. (China)* 48, 169–178.
- Tatarchuk, T., Paliychuk, N., Babu Bitra, R., Shyichuk, A., Naushad, M., Mironyuk, I., Ziolkovska, D., 2019. Adsorptive removal of toxic Methylene Blue and Acid Orange 7 dyes from aqueous medium using cobalt-zinc ferrite nanoadsorbents. *Desalin. Water Treat.* 150, 374–385.
- Wang, C., Wang, X., Jiang, X., Li, F., Lei, Y., Lin, Q., 2019a. The thermal behavior and kinetics of co-combustion between sewage sludge and wheat straw. *Fuel Process. Technol.* 189, 1–14.
- Wang, C., Li, G., Du, Y., Yan, Y., Li, H., Che, D., 2018. Ash deposition and sodium migration behaviors during combustion of Zhundong coals in a drop tube furnace. *J. Energy Inst.* 91 (2), 251–261.
- Wang, R., Zhao, Z., Qiu, L., Liu, J., 2017a. Experimental investigation of synergistic behaviors of lignite and wasted activated sludge during their co-combustion. *Fuel Process. Technol.* 156, 271–279.
- Wang, T., Hou, H., Ye, Y., Rong, H., Li, J., Xue, Y., 2019b. Combustion behavior of refuse-derived fuel produced from sewage sludge and rice husk/wood sawdust using thermogravimetric and mass spectrometric analyses. *J. Clean. Prod.* 222, 1–11.
- Wang, T., Xue, Y., Zhou, M., Yuan, Y., Zhao, S., Tan, G., Zhou, X., Geng, J., Wu, S., Hou, H., 2017b. Comparative study on the mobility and speciation of heavy metals in ashes from co-combustion of sewage sludge/dredged sludge and rice husk. *Chemosphere* 169, 162–170.
- Wei, B., Wang, X., Tan, H., Zhang, L., Wang, Y., Wang, Z., 2016. Effect of silicon–aluminum additives on ash fusion and ash mineral conversion of Xinjiang high-sodium coal. *Fuel* 181, 1224–1229.
- Xiang, R., Li, Y., Li, S., Xue, Z., He, Z., Ouyang, S., Xu, N., 2019. The potential usage of waste foundry sand from investment casting in refractory industry. *J. Clean. Prod.* 211, 1322–1327.
- Xie, C., Liu, J., Zhang, X., Xie, W., Sun, J., Chang, K., Kuo, J., Xie, W., Liu, C., Sun, S., Buyukada, M., Evrendilek, F., 2018. Co-combustion thermal conversion characteristics of textile dyeing sludge and pomelo peel using TGA and artificial neural networks. *Appl. Energy* 212, 786–795.
- Xu, Q., Ma, X., Yu, Z., Cai, Z., 2014. A kinetic study on the effects of alkaline earth and alkali metal compounds for catalytic pyrolysis of microalgae using thermogravimetry. *Appl. Therm. Eng.* 73 (1), 357–361.
- Yang, M., Xie, Q., Wang, X., Dong, H., Zhang, H., Li, C., 2018. Lowering ash slagging and fouling tendency of high-alkali coal by hydrothermal pretreatment. *Int. J. Min. Sci. Technol.* <https://doi.org/10.1016/j.ijmst.2018.05.007>.
- Yuan, X., He, T., Cao, H., Yuan, Q., 2017. Cattle manure pyrolysis process: kinetic and thermodynamic analysis with isoconversional methods. *Renew. Energy* 107, 489–496.
- Zhao, M., Raheem, A., Memon, Z.M., Vuppuladadiyam, A.K., Ji, G., 2019. Iso-conversional kinetics of low-lipid micro-algae gasification by air. *J. Clean. Prod.* 207, 618–629.